Wide Field of View Inversely Magnified Dual-Lens for Near-Field Submillimeter Wavelength Imagers

Gandini, Erio; Tamminen, Aleksi; Luukanen, Arttu; Llombart Juan, Nuria

DOI
10.1109/TAP.2017.2778016

Publication date
2018

Document Version
Accepted author manuscript

Published in
IEEE Transactions on Antennas and Propagation

Wide Field of View Inversely Magnified Dual-Lens for Near-Field Sub-Millimeter Wavelength Imagers

Erio Gandini, Aleksi Tamminen, Arttu Luukanen, and Nuria Llombart

***Abstract*—A wide field of view inversely magnified dual-lens system for sub-millimeter wavelength imagers is presented in this contribution. The antenna is designed for near-field focusing, at a range of 2.1 m from the primary aperture and to work in the frequency range from 200 to 600 GHz. The half power beamwidth is 0.27° (1 cm in the image plane) at 500 GHz, corresponding to a focused antenna directivity of approximately 55 dBi. The field of view is as large as ±25.4° (±1 m at the nominal range), corresponding to a scan range of ±100 half power beamwidths. The shapes of the lens surfaces are optimized to minimize the phase aberration loss over the entire scanning range. Moreover, the lenses are designed to be as thin as possible to limit the dielectric absorption loss. The directivity reduction of the edge pattern with respect to broadside is approximately 1 dB with an efficiency of 56%, making this lens an excellent candidate for imaging applications. The dual-lens system can be refocused by displacing the secondary lens and shows an essentially unchanged angular half power beamwidth over a refocusing range of ±50% with respect to the nominal imaging distance. A demonstrator was fabricated and the experimental results at 500 GHz confirm the predicted performance.**

***Index Terms*—Quasi-optical system, Sub-millimeter wavelength, passive imager.**

I. Introduction

THE European Union continues to want to improve the security in airports. Sub-millimeter wavelength imagers [1] represent promising instruments in this context because they are capable of detecting concealed objects on moving persons. Such imagers have been developed using active [2]-[3] and passive [4]-[6] configurations. Since only a few detectors coupled to focusing systems are used, these systems rely on high performance mechanical scanners for generating the images. The possibility of developing focal plane arrays (FPA) with several thousands of kinetic inductance detectors (KIDs) [7]-[9] opens a path for quasi-video rate and wide field of view (FOV) passive imagers.

Future security airport systems will require fast image rate ($\geq$ 10 Hz) and to operate in a scenario as in Fig. 1, where the image plane is located at relatively short distance, $R_f = 2.1$ m, from the aperture of the antenna. The required half power beam-width (HPBW) is in the order of 1 cm, 0.27° at the nominal range, corresponding to a focused antenna directivity (see the Appendix) of approximately 55 dBi. The FOV has to be compatible with a full body ($D_{FOV} = 2$ m), 50.8° at the nominal range. The edge pixel corresponds to a scan of 100 HPBWs.

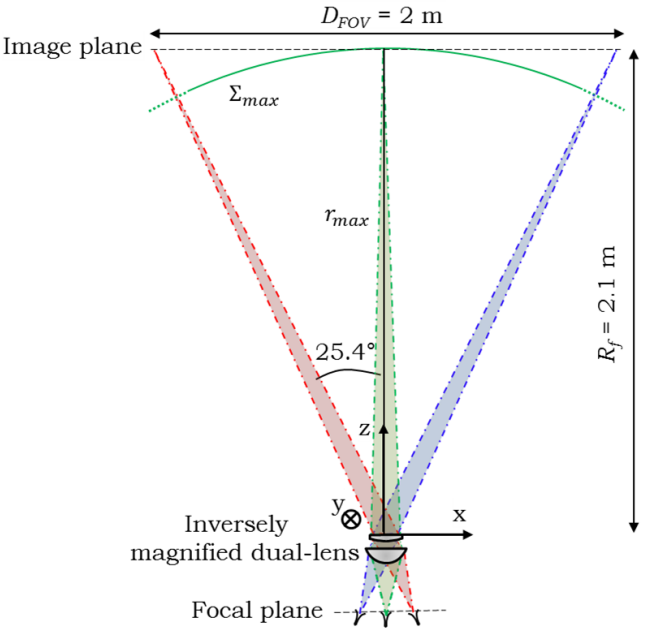

Fig. 1. Schematic representation of the proposed near-field imaging system.

The goal of this work is the development of a quasi-optical system that can fulfill the antenna system requirements for the described scenario. In particular, the proposed design can be coupled to the FPA described in [10], which operates over the frequency band ranging from 200 to 600 GHz. The two main challenges are represented by: i) the large FOV combined with very high directivity and near-field focusing; and ii) the wideband requirement. Since the quasi-optical system focuses in the Fresnel region, a mechanical based refocusing technique will also be implemented for allowing high quality image at different distances [11].

A. Wide Field of View Optics

In [12], a comparison table of the performance of the quasi-optical systems of the state-of-the-art imagers for security applications at sub-millimeter wavelengths was presented. The discussed scenario is well beyond previous implemented systems. Indeed, standard optical systems using conical surfaces cannot achieve these requirements. The effective FOV of a canonical symmetric elliptical reflector with the required

Erio Gandini and Nuria Llombart are with the department of Electrical Engineering, Mathematics and Computer Science of Delft University of Technology, Delft, The Netherlands (e-mail: E.Gandini, N.LlombartJuan@tudelft.nl). Aleksi Tamminen and Arttu Luukanen are with Asqella Oy, Helsinki, Finland.

The authors would like to thank the European Commission for the support to this work in the context of the Seventh Framework Programme (FP7) project Concealed Object Stand-Off Real-Time Imaging for Security (CONSORTIS), grant agreement no: 312745.

N. Llombart would like to thank the European Research Council for the starting grant LAA-THz-CC (639749).

HPBW is only 1 m wide at a 2 m range (see Fig 4(a) in [12]). The best reflector configuration, that leads to an effective FOV of 70% of a canonical reflector, was shown in [13] to be a Dragonian dual-reflector system [14]. However, the FOV of this solution is limited to about 20° (±10°) due to blockage effects associated to the dual-reflector configuration.

The path towards wide angular FOV quasi-optical systems is to use over-dimensioned optical components, with respect to diffraction limited optics, combined with properly shaped surfaces to reduce phase aberrations. This approach has been implemented for toroidal single reflectors, but it was limited to a single scanning direction [15] due to blockage and cross-polarization effects.

For this reason, the proposed architecture is a lens based system. In this case, no blockage occurs and, thanks to the lens symmetry, it allows the use of over-dimensioned optical components and shaped surfaces in all scanning planes. The drawback is the introduction of dielectric losses, which can become significant at sub-millimeter wavelengths. Therefore, a trade-off between the phase aberration, i.e. directivity, and dielectric losses will drive the optimization of the quasi-optical system.

The bandwidth requirement (200 to 600 GHz) does not allow the use of flat or Fresnel lenses since they are narrow band. Angular FOVs comparable to the one required in the current application were achieved by using aplanatic lenses [16], bifocal lenses [17], spherical lenses [18], dual-lenses [19] and other solutions with optimized surface shapes [20]-[23]. Most of these designs exploit curved FPAs to achieve low scanning loss. Moreover, the mentioned works describe quasi-optical systems focusing in the far field with much lower directivities than required, less than 40 dBi in all cases. In the considered scenario, an additional challenge is due to the near-field focusing configuration since both a linear phase (needed for scanning) and a quadratic phase (needed for focusing in the near-field) have to be controlled over the whole FOV, which is defined on a plane and not over a sphere.

The paper is structured as follows. The design and optimization of the proposed inversely magnified dual-lens is presented in Sec. II. The design considerations include both phase and dielectric losses and the performance is compared to a standard focusing lens. The refocusing capabilities of the dual-lens system are discussed in Sec. III and the experimental validation of the design at 500 GHz is shown in Sec. IV.

II. Inversely Magnified Dual-Lens Design

In this section, the design and performance of the proposed dual-lens design are reported and compared to a standard single lens system. It is known in optics, that the FOV can be enlarged by increasing the lens diameter and thickness, properly shaping its surfaces and adding focusing components [24]. In general, the thicker the lens the better the scanning performance because the path length error for the edge pixels can be partially compensated. However, the dielectric absorption loss becomes prohibitive at submillimetre-wavelengths for thick lenses.

A. Material Choice

The loss due to the lens material is caused by two main factors: reflection at the air-dielectric interfaces and dielectric absorption. High permittivity materials (i.e. silicon, $\epsilon_r \approx 12$) can have low absorption loss, but have large reflections. This can be alleviated by designing matching layers covering the surfaces of the lens. However, the fabrication of such layers is difficult in the current case since a large frequency bandwidth is required. Therefore, low permittivity materials are the preferred option, even if they present higher absorption loss. A material that was found to have good performance at submillimeter wave frequencies is TOPAS [25]. Its dielectric permittivity, ϵ_r, and the dielectric loss tangent, $\tan\delta$, have been measured using several samples [26]. It was found that their average values are: i) ϵ_r = 2.33, $\tan\delta$ = 5.16 $\times$ 10^{-4} at 250 GHz; and ii) ϵ_r = 2.33, $\tan\delta$ = 7.08 $\times$ 10^{-4} at 500 GHz. Considering a low loss material, it can be estimated that for a plane wave propagating normally into a TOPAS slab a maximum thickness of 4 cm can be used in order to have an absorption loss lower than 2 dB at 500 GHz.

B. Standard Focusing Lens

As a reference, a standard single lens focusing at the center of the image plane has been designed using two hyperbolic surfaces defined by their eccentricity and vertex distance. For both the faces of the lens, the eccentricity is $e = \sqrt{\epsilon_r}$. The vertex distances are defined as: $2a_f = 2F/(1+e)$ and $2a_t = 2R_f/(1+e)$, for the surfaces facing the feeds and the image plane, respectively. F and R_f are the distances between the lens and the focal plane and the imaging range, respectively.

The lens was dimensioned to achieve the required HPBW, $\Delta\theta = 0.55°$ and 0.27° at 250 and 500 GHz, respectively. The lens diameter, considering a uniform aperture illumination, can be calculated as D = 12.6 cm. Considering the curvature of the lens surfaces and allowing no space between their edges, the minimum central thickness is 2 cm. Such thickness is used here as it represents the configuration that minimizes the absorption loss. In order to evaluate the FOV of the lens, PO simulations were performed using GRASP [27] with the feed (a Gaussian beam with -10 dB taper at $\theta_e = 14.25°$, corresponding to an f-number of 2) displaced in the focal plane and tilted towards the center of the lens to minimize spillover.

The lens scanning performance was evaluated in terms of focused antenna directivity (Equation A.1 in the Appendix) and lens efficiency (Equation A.3 in the Appendix). These parameters at 500 GHz are plotted in Fig. 2 (solid lines) as a function of the scanning normalized by the nominal cross-range (i.e. projected over the FOV) HPBW, $\Delta\rho \approx \lambda R_f/D$. The standard lens guarantees good performance (less than 3 dB scan loss) for a very limited FOV, less than 50 HPBW (considering symmetric scanning: ±25 HPBW). This is insufficient for the scenario of Fig. 1, where a scan of ±100 HPBW is desired.

The 65% lens efficiency at broadside can be divided in three main factors: i) spillover loss, 0.4 dB; ii) absorption loss, approximately 1 dB; iii) reflections at the air-dielectric interfaces that can be estimated to be approximately 0.4 dB.

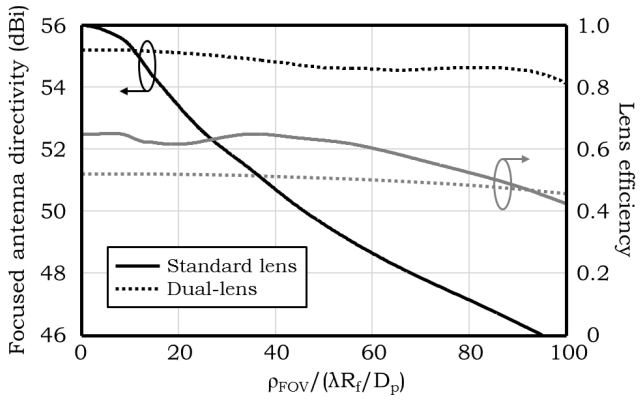

Fig. 2. Performance at 500 GHz as a function of the scanning in the image plane of the standard focusing lens of Sec. II-B and the inversely magnified dual-lens of Sec. II-C. The black and gray curves correspond to the focused antenna directivity and lens efficiency, respectively.

C. Inversely magnified dual-lens

The use of a dual-lens solution gives the advantage of enlarging the number of air-dielectric interfaces that can be used to minimize the phase aberration loss [24]. Here, we introduce the concept of inversely magnified dual-lens, whose geometry is shown in Fig. 3. In contrast with standard magnified quasi-optical systems [12], it consists of a primary lens dimensioned to achieve the required HPBW and a larger secondary lens. The use of a large secondary optic allows the optimization of the path lengths of the center and edge detectors differently because these feeds illuminate different parts of the lens.

Several techniques have been proposed in the literature for the optimization of lens shapes. In optics, the optimization is typically based on ray-tracing [24] and in microwave, similar ray-tracing solutions [28] or combination of ray-tracing and physical optics (PO) [29] are used. Although PO represents a more accurate technique, its application to the current optimization process would be impractical because of the large size of the optical elements being considered (the lens diameter is larger than 200 wavelengths at 500 GHz). Therefore, a technique based on ray-tracing is used here for the initial optimization. A PO analysis of the optimized geometry is then performed for a fine tuning of the performance and an accurate evaluation of the radiated field properties.

In order to minimize the phase aberration loss, the four surfaces of the lenses have to be optimized. Their profile is defined as a conic surface plus higher order polynomials

$$z = \frac{c\rho^2}{1+\sqrt{1-(1+k)c^2\rho^2}} + \sum_{i=1}^{8} \alpha_i \rho^{2i} \qquad (1)$$

where ρ and z are shown in Fig. 3, c is the curvature of the surface, k is the conic constant and α_ii are the weights of the terms of the polynomial expansion. The polynomial terms on the right of Equation (1) are used to shape the edge of the lens profiles. In particular, the surface shapes (S_{1s}, S_{2s}, S_{1p}, S_{2p} in Fig. 3) and the distances l and F were used as optimization variables. The thicknesses of the two lenses were also optimized, considering that the sum of the two should

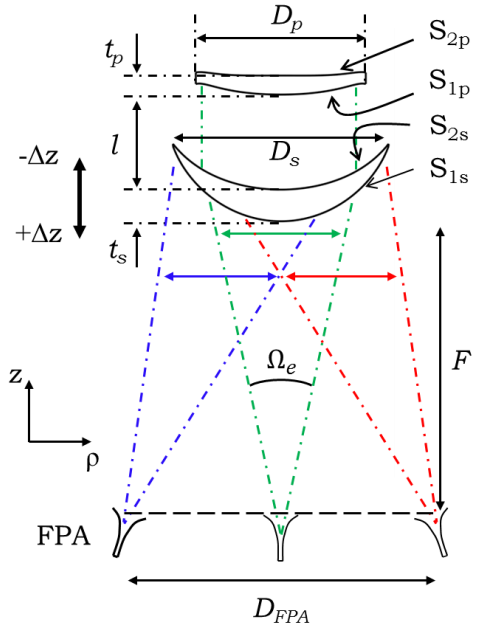

Fig. 3. Schematic view of the inversely magnified dual-lens system.

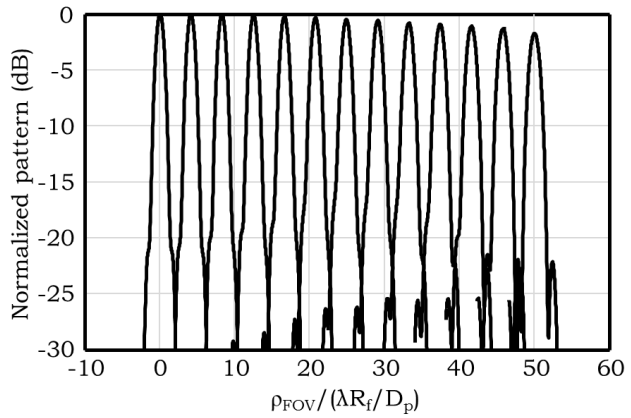

(a)

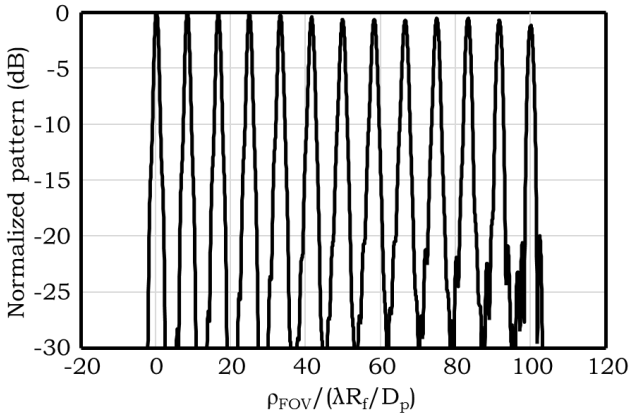

(b)

Fig. 4. Normalized patterns in the image plane of the inversely magnified dual-lens system: (a) 250 GHz, (b) 500 GHz.

TABLE I

GEOMETRICAL PARAMETERS OF THE DUAL LENS SYSTEM: (A) LENS AND SYSTEM SIZES, (B) SHAPE PARAMETERS OF THE SURFACE S_{1s}, (C) SHAPE PARAMETERS OF THE SURFACE S_{2s}, (D) SHAPE PARAMETERS OF THE SURFACE S_{1p}, (E) SHAPE PARAMETERS OF THE SURFACE S_{2p}.

(a)

D_p (mm)	D_s (mm)	t_p (mm)	t_s (mm)	l (mm)	F (mm)	D_{FPA} (mm)
134	170	15	25	75	226.5	240

(b)

c (mm^{-1})	k	α_1(mm^{-1})	α_2 (mm^{-3})	α_3 (mm^{-5})	α_4 (mm^{-7})	α_5 (mm^{-9})	α_6 (mm^{-11})	α_7 (mm^{-13})	α_8 (mm^{-15})
0.0097	0.340	9.7×10^{-4}	-1.9×10^{-8}	1.2×10^{-13}	-2.9×10^{-16}	3.7×10^{-20}	6.4×10^{-24}	-4.1×10^{-29}	-1.5×10^{-31}

(c)

c (mm^{-1})	k	α_1(mm^{-1})	α_2 (mm^{-3})	α_3 (mm^{-5})	α_4 (mm^{-7})	α_5 (mm^{-9})	α_6 (mm^{-11})	α_7 (mm^{-13})	α_8 (mm^{-15})
0.0136	-0.496	-3.2×10^{-3}	-4.4×10^{-8}	-5.2×10^{-14}	-3.4×10^{-16}	5.0×10^{-21}	3.8×10^{-24}	2.2×10^{-29}	-7.7×10^{-32}

(d)

c (mm^{-1})	k	α_1(mm^{-1})	α_2 (mm^{-3})	α_3 (mm^{-5})	α_4 (mm^{-7})	α_5 (mm^{-9})	α_6 (mm^{-11})	α_7 (mm^{-13})	α_8 (mm^{-15})
-0.0089	1.297	6.3×10^{-3}	4.1×10^{-7}	1.9×10^{-13}	3.3×10^{-15}	3.2×10^{-19}	-2.1×10^{-23}	-2.1×10^{-26}	-6.6×10^{-30}

(e)

c (mm^{-1})	k	α_1(mm^{-1})	α_2 (mm^{-3})	α_3 (mm^{-5})	α_4 (mm^{-7})	α_5 (mm^{-9})	α_6 (mm^{-11})	α_7 (mm^{-13})	α_8 (mm^{-15})
-0.0083	1.466	4.0×10^{-3}	5.0×10^{-7}	7.5×10^{-14}	1.7×10^{-15}	1.7×10^{-19}	-5.0×10^{-24}	-1.2×10^{-26}	-5.8×10^{-30}

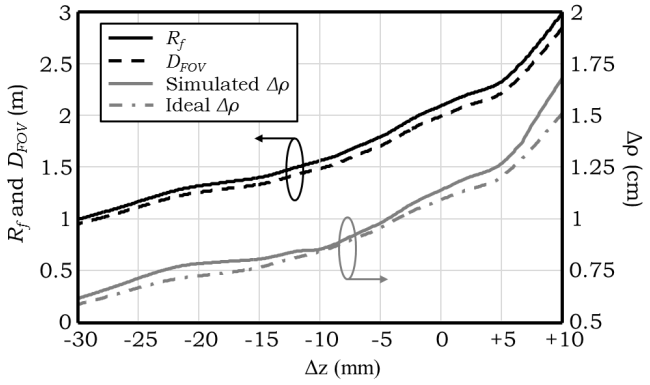

Fig. 5. Variation of the focusing range, FOV size and 3 dB beam projection on the image plane as a function of the displacement of the secondary lens.

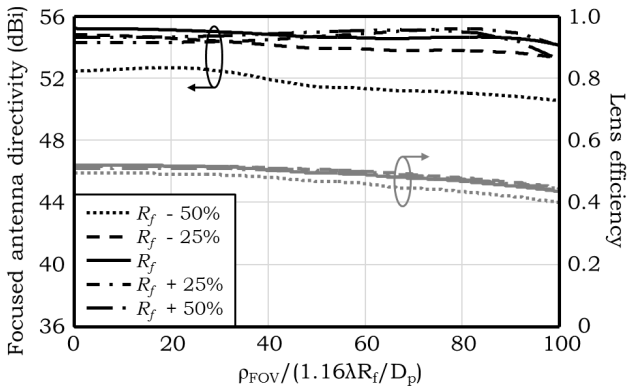

Fig. 6. Performance variation at 500 GHz as a function of the scanning for the considered refocusing ranges. The black and grey curves correspond to the focused antenna directivity and lens efficiency, respectively.

not exceed 4 cm to have low dielectric absorption (see Sec. II-A). The goals of the optimization are: i) minimization of the phase aberration loss, ii) synthesis of the desired effective f-number and iii) minimization of the beam deviation factor to allow a uniform distribution of the feeds along the FPA. The optimized geometrical parameters are summarized in Table I. In order to improve the scanning performance, the diameter of the primary and secondary lenses are both oversized compared to the nominal value of 12.6 cm.

The achieved focused antenna directivity and efficiency at 500 GHz as a function of the scanning in the image plane are shown in Fig. 2, dotted lines. The FOV enlargement obtained with the proposed dual-lens solution is achieved at the cost of introducing phase aberrations at broadside, corresponding to a directivity loss of almost 1 dB with respect to the standard lens of Sec. II-B. Despite the degraded performance at broadside, the optimized dual-lens allows to significantly alleviate the directivity reduction while scanning. The difference between the directivity at broadside and the one for 100 HPBW scan is as low as about 1 dB. The lens efficiency at broadside of the inversely magnified dual-lens is approximately 52%, slightly lower than the one of the single lens, because of the thicker dielectric and two additional air-dielectric interfaces. The discussed efficiency includes the spillover, that, in the current case, is defined over the solid angle $\Omega_e = 28.5°$ (see Fig. 3). The spillover loss depends on the feed and in this design is 0.4 dB (91% efficiency). Excluding this loss, the lens efficiency increases to 56%.

The normalized radiation patterns projected on the image plane of the inversely magnified dual-lens system are shown in Fig. 4 at 250 and 500 GHz. The projected HPBWs at broadside are 2.2 and 1.1 cm at the lower and higher frequencies, respectively. In both cases, the field at the edge of the scanning range is enlarged by a factor 1.3 and achieves the required specification for future security imagers.

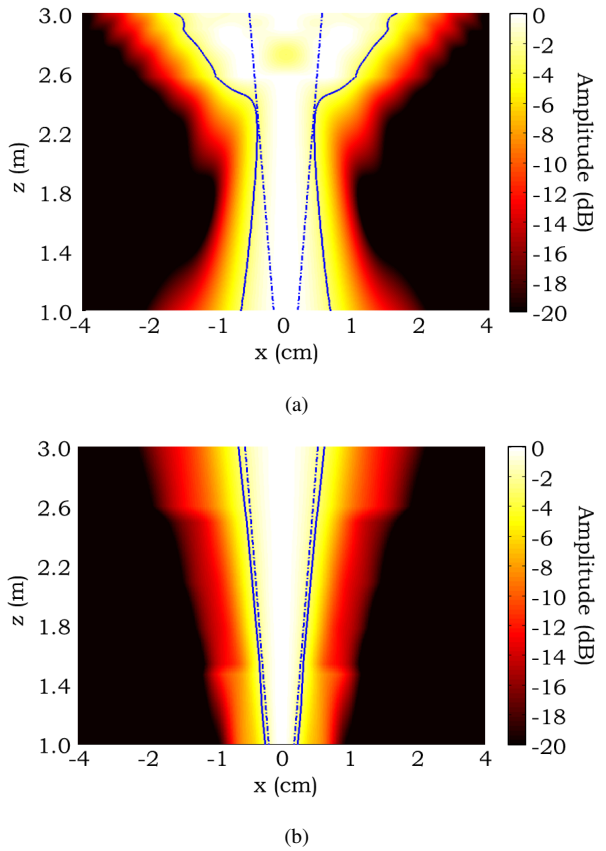

(a)

(b)

Fig. 7. xz-cut of the field scattered by the quasi-optical system: (a) no refocusing, (b) mechanical refocusing. The dot-dashed and solid lines correspond to the ideal and actual cross-range HPBW, respectively.

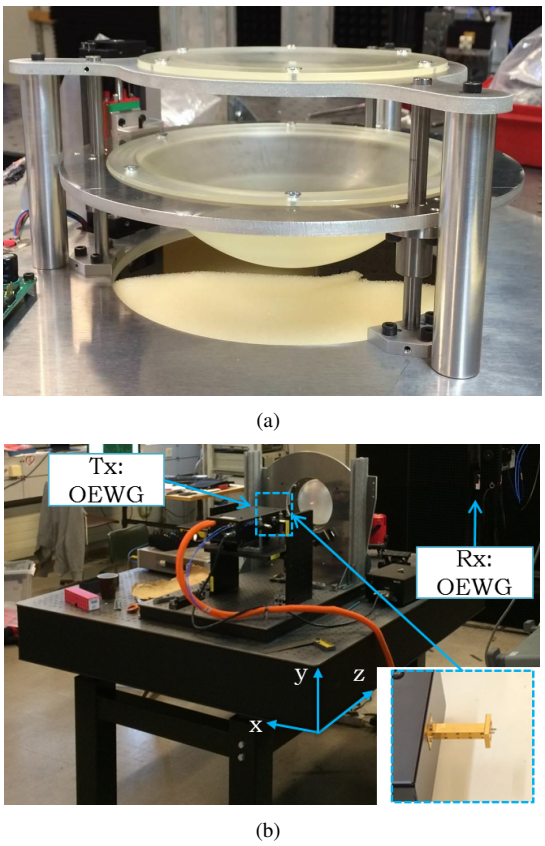

(a)

(b)

Fig. 8. Experimental configuration: (a) dual lens prototype, (b) measurement setup.

III. Refocused Lens Performance

Since the quasi-optical system is designed for focusing in the near-field, a refocusing mechanism has to be used to change its operational focusing range [11]. In the current case, the secondary lens can be displaced in the z-direction (see $\pm\Delta z$ in Fig. 3) in order to achieve an axial displacement of the image plane. If no additional aberrations are introduced, the quasi-optical system maintains the same angular HPWB and angular scanning range while refocusing. This behavior has two main effects when observing the fields projected in the image plane: the cross-range HPWB and FOV are narrowed/enlarged when the range is reduced/increased. The focusing range and linear FOV variation as a function of the secondary lens displacement are shown in Fig. 5, black curves. The considered refocusing range corresponds to $\pm 50\%$ with respect to the nominal focusing distance, $R_f = 2.1$ m. In Fig. 5, the variation of the cross-range HPBW ($\Delta\rho$) is also shown, grey curve. The achieved HPBW is compared to the one given by -10 dB aperture amplitude taper, i.e $1.16\lambda D$ [30]. The agreement between the simulated and ideal beam size is excellent over the consider ranges.

The variation of the focused antenna directivity and lens efficiency over the image plane is depicted in Fig. 6. The directivity variation while refocusing to ranges longer than the nominal one is stable and within 1 dB from the nominal results. The directivity is instead reduced by almost 3 dB for a 50% closer range. The lens efficiency does not show significant variations over the considered refocusing range.

The need for a mechanical refocus of the optics is shown in Fig. 7, where an xz-cut (see Fig. 1) of the field is depicted for a feed in the center of the focal plane. In case of non-refocused optics, Fig. 7(a), the field is collimated only over a small interval in the z-direction. Since the quasi-optical system is not focused, the field spreads rapidly while moving away from that area, degrading the resolution of the imaging system. Instead, when the secondary lens is displaced for refocusing, Fig. 7(b), the cross-range HPBW is very similar to the ideal one over the entire considered interval in the z-direction.

IV. Experimental Validation

A prototype of the quasi-optical system was fabricated and measured. The lenses were manufactured from TOPAS material using a lathe. A photograph of the prototype is shown in Fig. 8(a). The profiles of the fabricated lenses were measured and the maximum surface inaccuracy was found for S_{2s} and it is almost 100 μm at the edges. The measured inaccuracy was higher than specified, but its effects can be compensated by changing the secondary lens location, as shown below.

The antenna patterns were measured with a near-field xy-scanner, Fig. 8(b). The measurements were performed at 500 GHz, and the patterns were measured at the center of the image

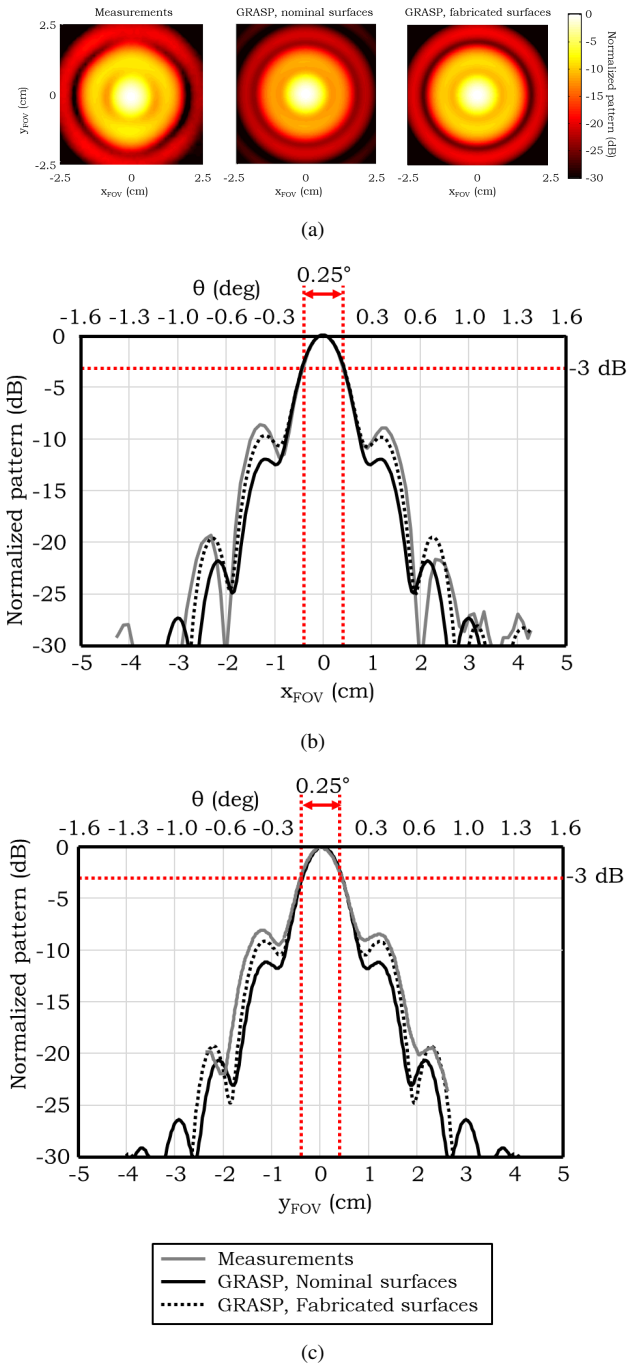

Fig. 9. Measured broadside patterns projected on the image plane at 500 GHz and R_f = 1.8 m: (a) 2D-pattern in the image plane (b) x-cut, (c) y-cut.

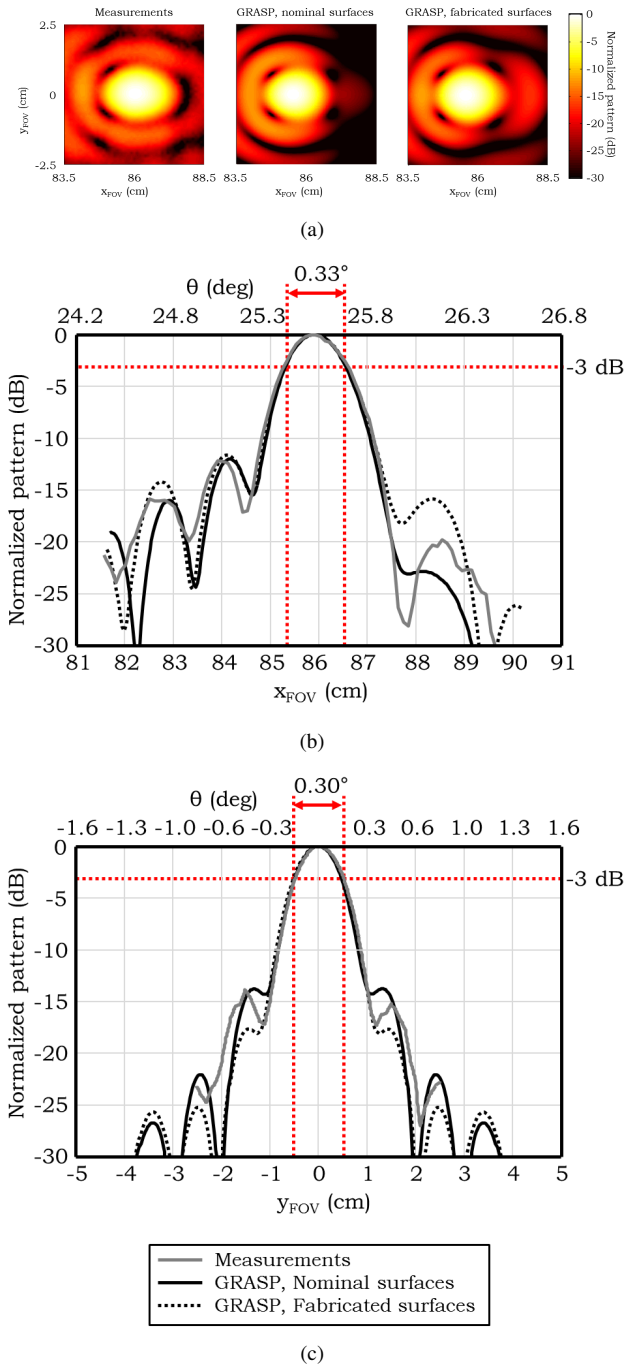

Fig. 10. Measured patterns for 100 HPBW scanning at 500 GHz and R_f = 1.8 m: (a) 2D-pattern in the image plane (b) x-cut, (c) y-cut.

plane for the three different ranges, R_f = 1.8, 2.1 and 2.5 m, whereas the scanning performance was evaluated only at the closest range. The nominal displacements of the secondary lens for the three different ranges are Δz = -4.5, 0, and +5 mm.

The proposed quasi-optical system can also be coupled to FPAs made of absorber based KIDS [9]. In order to reproduce the broad angular response of bare absorbers detectors, the measurements are done using open ended waveguides (OEWG) with size 0.56 × 0.28 mm^2 in both the focal and target planes. The photograph of the OEWG is shown in the inset of Fig. 8(b). The radiation of such probes has been simulated in GRASP by using a single mode OEWG, with the same dimensions, radiating on an infinite ground plane.

A. *Field Patterns In The Image Plane*

The measured and simulated patterns projected at the center and the edge of the image plane at the closest range, R_f = 1.8 m, are shown in Figs. 9 and 10, respectively, in the xy-plane (see Fig. 1) and the principal cuts (x and y-directions).

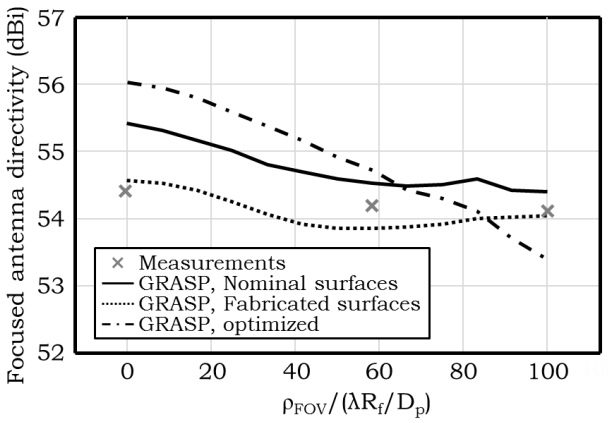

Fig. 11. Focused antenna directivity as a function of the scanning in the image plane at 500 GHz.

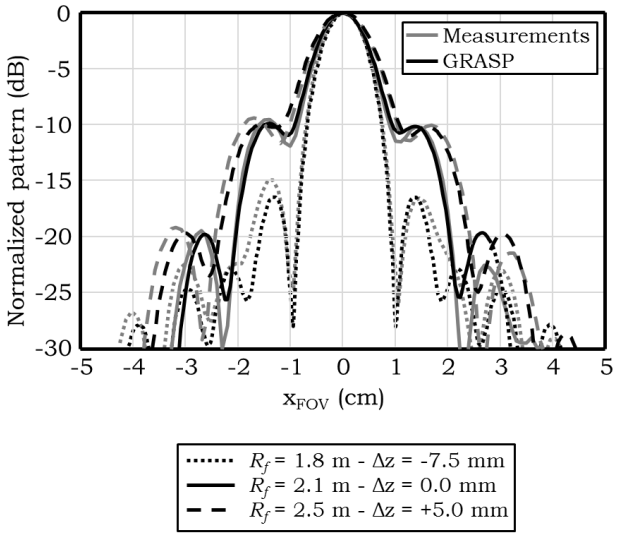

Fig. 12. Measured broadside patterns (x-cut) at 500 GHz at the ranges R_f = 1.8, 2.1 and 2.5 m. For R_f = 1.8 m, the position of the secondary lens is optimized to achieve the best focus at broadside.

The simulations were performed both considering the nominal and the fabricated surfaces of the lenses. The 2D-patterns, Fig. 9(a), show good symmetry for both simulations and measurements. The x and y-cuts show that the measured and simulated patterns are in excellent agreement when the fabricated surfaces are considered. The quasi-uniform illumination of the system causes an increase of the side lobe level (SLL) with respect to the cases in which a Gaussian feed was used to illuminate the optics (see Fig. 4). Considering the nominal designed surfaces, the SLL is acceptable, approximately -12 dB, for both the principal cuts. However, the inaccuracy of the fabricated surfaces results in an increase of the SLL to approximately -10 dB. The HPBW of the central pattern is, as expected, 0.25°. The HPBW of the edge pattern is 0.33° in the x direction, corresponding to an enlargement of a factor 1.3 compared to broadside.

The measured and simulated focused antenna directivities computed using (A.1) for the closest range ($R_f = 1.8$ m) of the designed dual-lens are reported in Fig. 11. The measurements (grey crosses) are in excellent agreement, within 0.3 dB, with the simulations including the measured surfaces (black dotted line). Because of the fabrication inaccuracy, the measured focused antenna directivity is reduced by 1 dB with respect to the nominal one (black solid line).

B. Refocusing

The measured patterns projected at the center of the image plane for the ranges $R_f = 2.1$ m and 2.5 m are shown in Fig. 12, solid and dashed lines, and compared to the corresponding GRASP simulations. The measured and simulated patterns are again in excellent agreement over the entire considered refocusing range.

The directivity at broadside can be maximized by using the refocusing capabilities of the dual-lens system. In particular, the pattern at the center of the image plane at $R_f = 1.8$ m, both simulated and measured, for the most focused case is reported in Fig. 12, dotted lines. The SLL is reduced to -15 dB and the focused antenna directivity is increased to approximately 56.5 dB (1 dB higher than the nominal case). Although the quality of the broadside patterns is improved, this configuration cannot be used in practice because the radiated beam at the edge of the image plane is severely affected, with a scan loss of 4 dB. An optimization of the lens position was performed to maximize the focused antenna directivity over the entire scanning range considering the measured lens surfaces. This allowed the reduction of the SLL at broadside to approximately -13 dB at the expenses of a 0.5 dB directivity reduction at the edge of the scanning range with respect to the original design. The optimized displacement of the secondary lens for $R_f = 1.8$ m is Δz = -7.5 mm and the simulated directivity for this configuration is reported in Fig. 11, black dot-dashed line.

C. Lens Efficiency

The lens efficiency does not depend on Δz (see Fig. 6), therefore it was evaluated for a single lens configuration (the one of Fig. 12) at 1.8 m range. The corresponding measurement setup is shown in Fig. 13 where a Pickett-Potter horn [31] with an aperture diameter of 4.6 mm and gain of 26.5 dB was used as receiving antenna. Considering that the receiving antenna is smaller than the size of the beam radiated by the lens system (10 mm), the incident field on the horn probe can be considered a local plane wave, therefore a expression similar to the Friis equation, as shown in (A.4), can be used to evaluate the ratio between the received and transmitted power, S_{21}. As indicated in Fig. 13, the lens efficiency, η_{lens}, can be divided in two terms, nominally, the feed dependent spillover efficiency, η_{SO}, and transmission efficiency, η_t. As in Sec. II, the spillover efficiency is calculated considering the feed radiation included in the solid angle $\Omega_e = 28.5°$. The transmission efficiency includes reflections at the air-dielectric interfaces and absorption loss. In the present configuration, the simulated focused antenna directivity and efficiencies are: D_{NF} = 56.5 dB, η_{SO} = 8.6% and η_t = 60%. The S_{21}

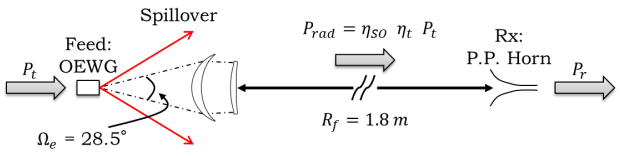

Fig. 13. Considered setup for the efficiency evaluation.

calculated by using (A.4) is -21.3 dB and verified numerically, whereas the measured one is higher and equal to -19.4 dB. The main reason of the discrepancy is the lack of a measured and calibrated OEWG model at this frequency, which may lead to inaccuracies in the order of a few dBs in the spillover at the first lens. Therefore, the difference in the measured and simulated S_{21} is within the expected accuracy.

V. Conclusion

In this contribution, an inversely magnified dual-lens antenna system at sub-millimeter wavelengths was presented. It was designed to work in the frequency bandwidth ranging from 200 to 600 GHz and to focus in the near-field at a distance of 2.1 m from the primary aperture.The design challenges related to the large scanning range with high focused antenna directivity and high efficiency were discussed in details. The design achieved a focused antenna directivity of approximately 55 dBi at the center of the field of view. At the edge of the considered scanning range of ± 100 HPBW (50.8° angular field of view) a directivity reduction of approximately 1 dB was obtained. The HPBW for such large scanning angles is enlarged by only a factor 1.3, allowing the use of the quasi-optical system in security imagers with a constant resolution over a FOV of more than 30000 HPBWs. The efficiency of the dual-lens system, excluding the feed dependent spillover loss, is 56%. A mechanical refocusing mechanism based on the displacement of the secondary lens was also presented. Results comparable to the ones at the nominal focusing distance were obtained for a refocusing range of $\pm 50\%$. The predicted performance was successfully confirmed experimentally for several ranges and over the entire field of view.

Acknowledgment

The authors would like to thank the Aalto University Department of Radio Science and Engineering for offering their near-field measurement facilities for this work.

Appendix

In order to evaluate the quality of the near-field focused patterns (converging spherical wave), we can use a parameter, referred here as focused antenna directivity, similar to the directivity commonly used for far field operating antennas (diverging spherical field) as it was defined in [32]. This focused antenna directivity is evaluated at the image plane (in the radiative near-field region) in the location of the maximum of the radiated field, $\vec{r}_{max}$ using the same expression that is used for the far field:

$$D_{NF} = \frac{4\pi \mid \vec{S}_a(\vec{r}_{max}) \mid r_{max}^2}{P_{rad}} \tag{A.1}$$

where $\vec{S}_a(\vec{r}_{max})$ is the active component of the Poynting vector and P_{rad} is the power radiated by the lens, over an hemisphere, Σ_{max} in Fig. 1, centered at the lens and radius r_{max}. Note that this value of near-field directivity is only valid at that specific observation point.

Since the field, at the focus of a quasi-optical system, is locally a plane wave, the power density crossing the image plane can be expressed as:

$$\vec{S}_a(\vec{r}_{max}) = \frac{1}{2\eta_0} \mid \vec{E}_a(\vec{r}_{max}) \mid^2 \hat{r} \tag{A.2}$$

where $\vec{E}_a(\vec{r}_{max})$ is the electric field orthogonal to$\hat{r}_{max}$ (direction of the maximum of the radiated field, see Fig. 1).

In order to evaluate the antenna focused gain, we need to introduce the lens efficiency, which is calculated as follows:

$$\eta_{lens} = \frac{P_{rad}}{P_t} \tag{A.3}$$

where P_t is the total power radiated by the feed.

Both (A.1) and (A.3) are useful to express the power budget of a near-field link in terms of standard far-field quantities (i.e. Friis equation). In particular, if the receiving antenna is significantly smaller than the size of the field radiated by the lens in the image plane, the incident field can be regarded as a local plane wave and the received power can be evaluated as $P_r = \mid \vec{S}_a \mid A_{eff}$, with A_{eff} being the effective area of the receiving antenna. In this case, the ratio between the received and transmitted power, S_{21}, can then be calculated by using the following expression:

$$S_{21} = \frac{P_r}{P_t} = \eta_{lens} D_{NF} G_{rx} \left(\frac{\lambda}{4\pi r_{max}} \right)^2 \tag{A.4}$$

where G_{rx} is the gain of the receiving antenna and λ is the wavelength. Eq (A.4) applies when the lens is in the far field of the receiving antenna.

References

[1] R. Appleby and H. B. Wallace, "Standoff detection of weapons and contraband in the 100 GHz to 1 THz region," *IEEE Trans. Antennas Propag.*, vol. 55, no. 11, pp. 2944-2956, Nov. 2007.

[2] K.B. Cooper, R.J. Dengler, N. Llombart, T. Bryllert, G. Chattopadhyay, P. H. Siegel, "THz imaging radar for standoff personnel screening," *IEEE Trans. Terahertz Science Tech.*, vol. 52, no. 5, pp. 251-259, Sep. 2010.

[3] J. Grajal, A. Badolato, G. Rubio-Cidre, L. Ubeda-Medina, B. Mencia-Oliva, A. Garcia-Pino, B. Gonzalez-Valdes, and O. Rubiños , "3-D High-Resolution Imaging Radar at 300 GHz With Enhanced FoV," *Trans. Microwave Theory and Tech*, vol. 63, no.3, pp. 1097-1107, Mar. 2015.

[4] E. Grossman, C. Dietlein, J. Ala-Laurinaho, M. Leivo, L. Gronberg, M. Gronholm, P. Lappalainen, A. Rautiainen, A. Tamminen, and A. Luukanen, "Passive terahertz camera for standoff security screening," *Applied Optics*, vol. 49, no. 19, pp. E106-E120, Jul. 2010.

[5] E. Heinz, T. May, D. Born, G. Zieger, K. Peiselt, V. Zakosarenko, T. Krause, A. Krüger, M. Schulz, F. Bauer, and H.-G. Meyer, "Progress in Passive Submillimeter-wave Video Imaging," *Proc. SPIE*, Jun. 2014.

[6] S. Rowe, E. Pascale, S. Doyle, C. Dunscombe, P. Hargrave, A. Papageorgio, K. Wood, P. A. R. Ade, P. Barry, A. Bideaud, T. Brien, C. Dodd, W. Grainger, J. House, P. Mauskopf, P. Moseley, L. Spencer, R. Sudiwala, C. Tucker, and I. Walker, "A passive terahertz video camera based on lumped element kinetic inductance detectors," *AIP Review of Scientific Instruments*, 87, 033105-1, Mar. 2016.

[7] P. K. Day, H. G. Le Duc, B. A. Mazin, A. Vayonakis, and J. Zmuidzinas, "A broadband superconducting detector suitable for use in large arrays," *Nature*, vol. 425, no. 6960, pp. 817-821, Oct. 2003.

[8] J. J. A Baselmans, J. Bueno, S. J. C. Yates, O. Yurduseven, N. Llombart, K. Karatsu, A. M. Baryshev, L. Ferrari, A. Endo, D. J. Thoen, P. J. de Visser, R. M. J. Janssen, V. Murugesan, E. F. C. Driessen, G. Coiffard, J. Martin-Pintado, P. Hargrave, and M. Griffin, "A kilo-pixel imaging system for future space based far-infrared observatories using microwave kinetic inductance detectors," *arXiv:1609.01952v1*, Sep. 2016.

[9] A. Timofeev, J. Luomahaara, L. Gronberg, A. Mayra, H. Sipola, M. Aikio, M. Metso, V. Vesterinen, K. Tappura, J. Ala-Laurinaho, A. Luukanen, and J. Hassel, "Optical and Electrical Characterization of a Large Kinetic Inductance Bolometer Focal Plane Array," *IEEE Trans. Thz Science Tech.*, 2017.

[10] S. O. Dabironezare, J. Hassel, L. Grnberg, E. Gandini, A. Neto, and N. Llombart, "Optimization Of Frequency Selective Absorbers For Sub-mm Security Imagers," *IRMMW-THz 2016*, Copenhagen, Denmark, Sep. 2016.

[11] N. Llombart and B. Blazquez, "Refocusing a THz imaging radar: implementation and measurements," *IEEE Trans. Antennas Propag.*, vol. 62, no.3, pp. 1529-1534, Mar. 2014.

[12] E. Gandini, J. Svedin, T. Bryllert, and N. Llombart, "Opto-mechanical system design for dual-mode stand-off submillimeter wavelength imagers," *IEEE Trans. Thz Science Tech.*, Early Access, May 2017.

[13] E. Gandini and N. Llombart, "Toward a real time stand-off submillimeter-wave imaging system with large field of view: quasi-optical system design considerations," *Proc. SPIE*, vol. 9462, Apr. 2015.

[14] C. Dragone, "Unique reflector arrangement with very wide field of view for multibeam antennas," *Electron. Lett.*, vol. 19, no. 25/26, pp. 10611062, Dec. 1983.

[15] W. P. Craig, C. M. Rappaport, and J. S. Mason, "A high efficiency, wide-angle scanning offset reflector antenna," *IEEE Trans. Antennas Propag.*, vol. 41, no. 11, pp. 1481-1490, Nov 1993.

[16] G. C. Cloutier and G. Bekefi, "Scanning characteristics of microwave aplanatic lenses," *IRE Trans Antennas Propag.*, vol. 5, no. 4, pp. 391-396, Oct. 1957.

[17] A. L. Peebles, "A dielectric bifocal lens for multibeam antenna applications," *IEEE Trans Antennas Propag.*, vol. 36, no. 5, pp. 599-606, May 1988.

[18] B. Schoenlinner, X. Wu, J. P. Ebling, G. V. Eleftheriades, and G. M. Rebeiz, "Wide-scan spherical-lens antennas for automotive radars," *IEEE Trans. Microwave Theory Tech.*, vol. 50, no. 9, pp. 2166-2175, Sep 2002.

[19] N. T. Nguyen, A. V. Boriskin, L. Le Coq, and R. Sauleau, "Improvement of the scanning performance of the extended hemispherical integrated lens antenna using a double lens focusing system," *IEEE Trans. Antennas Propag.*, vol. 64, no. 8, pp. 3698-3702, Aug. 2016.

[20] C. M. Rappaport and A. I. Zaghloul, "Optimized three-dimensional lenses for a wide-angle scanning," *IEEE Trans. Antennas Propag.*, vol. AP-33, no. 11, pp. 1227-1236, Nov. 1985.

[21] Y. Tajima and Y. Yamada, "Design of shaped dielectric lens antenna for wide angle beam steering," *Electronics and Communications in Japan*, part 3, vol. 89, no. 2, 2006.

[22] T. Maruyama, K. Yamamori, and Y. Kuwahara, "Design of multibeam dielectric lens antennas by multiobjective optimization," *IEEE Trans. Antennas Propag.*, vol. 57, no. 1, pp. 57-63, Jan. 2009.

[23] J. R. Costa, M. G. Silveirinha, and C. A. Fernandes, "Evaluation of a double-shell integrated scanning lens antenna," *IEEE Antennas Wireless Propag. Letters*, vol. 7, pp. 781-784, 2008.

[24] W. J. Smith, "Modern optical engineering Fourth edition," *SPIE Press, Ed. Mc Graw Hill*, ISBN: 978-0-07-147687-3, 2008.

[25] http://www.topas.com/sites/default/files/files/optical_e.pdf.

[26] D. A. Robertson, University of St Andrews, "Private communications," 2016.

[27] TICRA, GRASP v 10.5, 2015.

[28] B. Chantraine-Bares, R. Sauleau, L. Le Coq, and K. Mahdjoubi, "A new accurate design method for millimeter-wave homogeneous dielectric substrate lens antennas of arbitrary shape," *IEEE Trans. Antennas Propag.*, vol. 53, no. 3, pp. 1069-1082, Mar. 2005.

[29] R. Sauleau and B. Bares, "A complete procedure for the design and optimization of arbitrarily shaped integrated lens antennas," *IEEE Trans. Antennas Propag.*, vol. 54, no. 4, pp. 1122-1133, Apr. 2006.

[30] P. F. Goldsmith, "Quasioptical systems: Gaussian beam quasioptical propagation and applications," Wiley-IEEE Press, ISBN: 978-0-7803-3439-7, 1997.

[31] P. D. Potter, "A new horn antenna with suppressed sidelobes and equal beamwidth," *JPL Technical Report.*, no. 32-354, Feb. 1963.

[32] R. C. Hansen, "Focal region characteristics of focused array antennas," *IEEE Trans. Antennas Propag.*, vol. AP-33, no. 12, pp. 1328-1337, Dec. 1985

Erio Gandini received the M.Sc. degree in electrical engineering from the University of Modena and Reggio Emilia, Modena, Italy and the PhD degree in Electrical Engineering from the University of Rennes 1 in 2009 and 2012, respectively. In 2011 he was a visiting PhD student at the University of Michigan. In January 2013 he joined the Ecole polytechnique fédérale de Lausanne (EPFL), Lausanne, Switzerland. In October 2013 he joined the THz sensing group at the Delft University of Technology, Delft, the Netherlands, where he currently working as research scientist. Since 2016 he is working as Antenna Scientist in the radar department of TNO Defence, Security and Safety, The Hague, The Netherlands. Erio Gandini scientific activities are in the broad area of applied electromagnetics. His research interests include quasi-optical systems, phased array antennas, sub-millimeter and terahertz imaging systems, frequency selective surfaces, beam-forming networks.

Aleksi Tamminen was born in Ruotsinpyhtää, Finland, in 1982. He received the B.Sc. (Tech.) and M.Sc. (Tech.) degrees from the Helsinki University of Technology (TKK), Espoo, Finland, in 2005 and 2007. He received the Lic.Sc. (Tech.) and the Doctor of Science (Tech.) degrees in 2011 and 2013 from Aalto University (former TKK Helsinki University of Technology). From 2005 to 2013, he was with the Department of Radio Science and Engineering at Aalto University. He has been involved with submillimeter- and millimeter-wave projects, especially with imaging, antenna measurements, and reflectarrays. Currently, Dr. Tamminen is with Asqella Ltd and continues on working with submillimeter-wave imaging systems.

Arttu Luukanen (born 1972, native of Finland) received his M.Sc. degree from the University of Helsinki, Finland in applied physics in 1999. He was awarded a Ph.D. in 2003 from the University of Jyväskylä, Finland, also in applied physics. After this he joined the VTT Technical Research Centre of Finland as a research scientist. From late 2003 until 2005 he worked as a guest researcher at the National Institute of Standards and Technology in Boulder, Colorado, U.S.A. In 2005, he was appointed as the director of MilliLab the Millimetre-wave Laboratory of Finland, and in 2009 as the Research Professor of Micro and Nanosystems at VTT. From 2007 until 2012, Dr Luukanen served on the International Advisory Board of the Swedish FOI-FOCUS Centre of Excellence on Sensors, Multisensors and Sensor networks, and from 2013 onwards on the International Advisory Board of the Chalmers GHz Centre. In 2013 he co-founded Asqella Ltd to commercialize passive multi-band submillimetre-camera technology, a long time subject of his research. Currently, Dr Luukanen serves as the Managing Director of Asqella. He is also an elected member of the Finnish Academy of Technical Sciences. His current research interests include mm-wave and THz devices, circuits and imaging systems as well as turning research into profitable business.

Nuria Llombart (S06M07SM13) received the Electrical Engineering and Ph.D. degrees from the Polytechnic University of Valencia, Spain, in 2002 and 2006, respectively. During her Master's degree studies she spent one year at the Friedrich-Alexander University of Erlangen-Nuremberg, Germany, and worked at the Fraunhofer Institute for Integrated Circuits, Erlangen, Germany. From 2002 until 2007, she was with the Antenna Group, TNO Defence, Security and Safety Institute, The Hague, The Netherlands, working as a Ph.D. student and afterwards as a Researcher. From 2007 until 2010, she was a Postdoctoral Fellow at the California Institute of Technology, working for the Sub millimeter Wave Advance Technology Group, Jet Propulsion Laboratory, Pasadena, USA. She was a Ramn y Cajal Fellow at the Optics Department of the Complutense University of Madrid, Spain, from 2010 to 2012. In September 2012, she joined the THz Sensing Group at the Technical University of Delft, The Netherlands, where she is currently an Associate Professor. She has co-authored over 150 journal and international conference contributions. Her research interests include the analysis and design of planar antennas, periodic structures, reflector antennas, lens antennas, and waveguide structures, with emphasis in the THz range. Dr. Llombart was co-recipient of the H.A. Wheeler Award for the Best Applications Paper of the year 2008 in the IEEE Transactions on Antennas and Propagation, the 2014 THz Science and Technology Best Paper Award of the IEEE Microwave Theory and Techniques Society and several NASA awards. She also received the 2014 IEEE Antenna and Propagation Society Lot Shafai Mid-Career Distinguished Achievement Award. She serves as a Board Member of the IRMMW-THz International Society. In 2015, she was awarded with an European Research Council (ERC) Starting Grant.